

Screening Polarimetric SAR Data via Geometric Barycenters for Covariance Symmetry Classification

Luca Pallotta^{1b}, *Senior Member, IEEE*, and Manlio Tesauro

Abstract—This letter proposes a robust framework for polarimetric covariance symmetries classification in synthetic aperture radar (SAR) images applying a prescreening on the data looks before they are used to perform inferences. More specifically, the devised method improves the performance of a previous work based on the exploitation of the special structures assumed by the covariance/coherence matrix when symmetric scattering mechanisms dominate the polarimetric returns. To do this, the algorithm selects first the most homogeneous data through the cancellation of those sharing the highest generalized inner product (GIP) values computed with the use of the geometric barycenters. Then, the procedure based on model order selection (MOS) developed in the homogeneous case is applied on the filtered data. The conducted tests show the potentiality of the proposed method in correctly classifying the observed scene of L-band real-recorded SAR data with respect to its standard counterpart.

Index Terms—Covariance and coherence scattering matrix, geometric barycenter, information geometry, outlier cancellation, polarimetric synthetic aperture radar (SAR), unsupervised classification.

I. INTRODUCTION

POLARIMETRY is a remarkable tool often used in the context of Synthetic aperture radar (SAR) processing and application. In fact, a multitude of research works using polarimetry to enhance detection and/or classification capabilities are continuously published. In this respect, the polarimetric covariance/coherence matrix finds its space of action in many algorithms or procedures to extract more and more information about the observed scene [1], [2], [3], [4], [5], [6], [7], [8], [9]. Nghiem et al. [2] have shown that the polarimetric covariance assumes special structures when some symmetric scattering mechanisms impact on the polarimetric returns. In this respect, a framework capable of identifying the above-mentioned scattering symmetries has been developed in [7], exploiting the structure shared by the covariance (or coherence) matrix. The derived problem is a composite hypothesis test including nested instances solved resorting to the model order selection (MOS) rules [10], [11], [12]. To be precise, for each pixel under test, a neighborhood assumed to share some homogeneity properties (i.e., the same spectral properties) is

Manuscript received 9 November 2022; revised 24 January 2023; accepted 25 February 2023. Date of publication 1 March 2023; date of current version 10 March 2023. (*Corresponding author: Luca Pallotta.*)

The authors are with the School of Engineering, University of Basilicata, 85100 Potenza, Italy (e-mail: luca.pallotta@unibas.it; manlio.tesauro@unibas.it).

Digital Object Identifier 10.1109/LGRS.2023.3250741

extracted before the MOS computation. Unfortunately, for real SAR images, the homogeneity assumption for the pixel in the neighborhood cannot be often considered valid due to the presence of outliers, power variations, noise spikes, speckle, point-like targets, and so on, with a consequent classification performance degradation.

To overcome this drawback, this letter proposes an enhanced algorithm aimed at improving the symmetry classification performance of the method developed in [7] performing a prescreening of the most homogeneous neighboring looks before the MOS computation. This operation is conducted excising the pixels sharing the highest values of the generalized inner product (GIP) computed using the geometric barycenters as covariance estimates [13]. Tests conducted on real-recorded L-band data have shown the effectiveness of the proposed method that overcomes the standard one developed for homogeneous scenes.

The remainder of the letter is organized as follows. In Section II, the problem is introduced, and the proposed algorithm is described in detail. Section III discusses results obtained on the L-band SAR data. Finally, Section IV concludes the letter.¹

II. PROBLEM FORMULATION AND ALGORITHM DESCRIPTION

In this letter, we propose an enhanced algorithm for covariance symmetries' classification after a proper selection of the most homogeneous looks within the neighborhood of the pixel under test. The algorithm, starting from the full-polarimetric SAR image, for each pixel under test, extracts its neighborhood through a sliding window. Then, the most homogeneous looks are screened applying the outlier cancellation procedure based on the GIP developed in [13] for radar detection purposes. Once the most homogeneous data looks

¹*Notation:* We use boldface for vectors \mathbf{a} (lower case) and matrices \mathbf{A} (upper case). The conjugate and conjugate transpose operators are denoted by the symbols $(\cdot)^*$ and $(\cdot)^\dagger$, respectively. $\text{tr}(\cdot)$ and $\det(\cdot)$ are, respectively, the trace and the determinant of the square matrix argument. $\mathbf{diag}(\mathbf{a})$ indicates the diagonal matrix whose i th diagonal element is the i th entry of \mathbf{a} . The letter j represents the imaginary unit, and for any complex number x , $|x|$ represents its modulus. For a matrix \mathbf{A} , whose eigenvalue decomposition is $\mathbf{A} = \mathbf{U}_A \mathbf{diag}(\boldsymbol{\lambda}_A) \mathbf{U}_A^\dagger$, with \mathbf{U}_A the unitary matrices containing its eigenvectors and $\boldsymbol{\lambda}_A = [\lambda_1^A, \dots, \lambda_N^A]$ the vector of the corresponding eigenvalues, we define $\log \mathbf{A} = \mathbf{U}_A \mathbf{diag}(\boldsymbol{\lambda}_A^L) \mathbf{U}_A^\dagger$ with $\boldsymbol{\lambda}_A^L = [\log(\lambda_1^A), \dots, \log(\lambda_N^A)]$, $\exp \mathbf{A} = \mathbf{U}_A \mathbf{diag}(\boldsymbol{\lambda}_A^E) \mathbf{U}_A^\dagger$, with $\boldsymbol{\lambda}_A^E = [\exp(\lambda_1^A), \dots, \exp(\lambda_N^A)]$, and $\mathbf{A}^\alpha = \mathbf{U}_A \boldsymbol{\Lambda}_A^\alpha \mathbf{U}_A^\dagger$ with $\alpha \in \mathbb{R}^+$. Finally, $\mathbf{L}(\mathbf{A})$ indicates the Cholesky decomposition [14, p. 114] of the matrix \mathbf{A} .

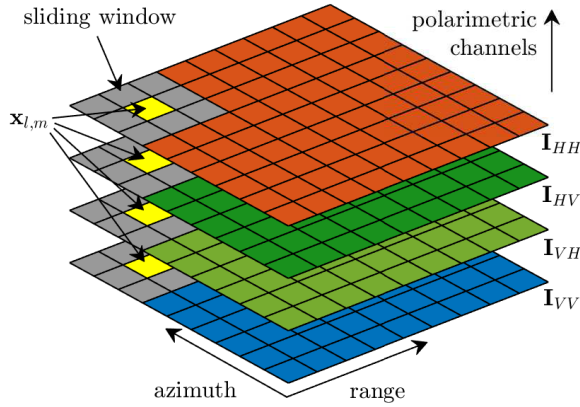


Fig. 1. Datacube of the full-polarimetric SAR images.

are selected, their sample matrix is computed and used as input to the covariance symmetry detection procedure of [7]. Sections II-A–II-D provide a deep description of all the steps composing the proposed framework.

A. Polarimetric SAR Datacube Formation

The input of the algorithm is the full-polarimetric SAR image of the observed scene arranged to form a datacube as illustrated in Fig. 1. More precisely, for each pixel to analyze, $N = 4$ complex returns associated with each of the four polarimetric channels, say I_{HH} , I_{HV} , I_{VH} , and I_{VV} , are recorded. Hence, the N measurements associated with the same pixel are saved in $X(l, m)$, $l = 1, \dots, L$ and $m = 1, \dots, M$ (L and M are the azimuth/range sizes of the image) to obtain a 3-D datacube X of size $L \times M \times N$. Therefore, the proposed method extracts a rectangular neighborhood \mathcal{A} of size $K = W_1 \times W_2 \geq N$ for each pixel under test. The subset of pixels representing the small datacube extracted through \mathcal{A} is organized in matrix form, indicated with \mathbf{R} , where each column is the polarimetric vector of each return in \mathcal{A} contained. Then, \mathbf{R} is modeled as a random matrix, whose columns, $\mathbf{r}_1, \dots, \mathbf{r}_K$, are modeled as independent and identically distributed (i.i.d.) zero-mean circular complex Gaussian random vectors with covariance \mathbf{M} .

B. Homogeneous Data Looks Screening Procedure

The screening procedure presented in this section is aimed at selecting the most homogeneous looks contained in the sliding window. Hence, starting from the K data looks in the neighborhood of the pixel under test, it rejects the κ_0 vectors sharing the highest GIP values [15], [16], [17]. Following the lead of [13], the GIP is herein computed with the geometric barycenters (described in the next subsection) for their selective capabilities in the space of positive definite matrices. To this aim, we indicate with $\Omega = \{1, 2, \dots, K\}$ the set of indices for all the available looks, and with $\Omega_0 = \{k_1, k_2, \dots, k_{K-\kappa_0}\} \subseteq \Omega$ the subset (of size $\bar{K} = K - \kappa_0$) of the looks selected after the excision process. Hence, the data screening method comprises the following two main steps. First, starting from the available K looks, $\mathbf{r}_1, \dots, \mathbf{r}_K$, their

covariance matrix is estimated as the geometric barycenter $\widehat{\mathbf{M}}_d$ having fixed a specific distance $d(\cdot, \cdot)$ in the space of positive definite covariance matrices (this estimation procedure is explained in Section II-C). The second step evaluates the following quadratic form (dubbed GIP) for each single data contained within the set Ω , that is,

$$\rho_k^{(d)} = \mathbf{r}_k^\dagger \widehat{\mathbf{M}}_d^{-1} \mathbf{r}_k, \quad k = 1, \dots, K. \quad (1)$$

Once $\rho_k^{(d)}$, $k = 1, \dots, K$, is computed, it needs to be sorted in decreasing order and stored in the vector $\boldsymbol{\rho}^{(d)}$. Finally, all the κ_0 data looks showing the highest values of GIP in $\boldsymbol{\rho}^{(d)}$ are canceled, namely, the set Ω_0 of the selected $\bar{K} = K - \kappa_0$ indices is derived. Since the GIP can measure the energy of the vector $\widehat{\mathbf{M}}_d^{-(1/2)} \mathbf{r}_k$, the selection algorithm removes the κ_0 looks containing the highest energy in the so-called quasi-whitened space. This motivates the application of this procedure for data screening.

1) *Adaptive Selection of the Parameter κ_0* : Before choosing the parameter κ_0 , it is worth observing that it rules the tradeoff between the amount of outliers to excise and the remaining homogeneous looks used for the next sample covariance estimation process. In fact, increasing κ_0 allows for a better outliers' cancellation at the expense of a poor sample covariance estimate because of the reduced number of sample data. For these reasons, the prior set of the parameter κ_0 is not a simple task, and so there is the need to resort to its adaptive selection. Hence, the considered adaptive procedure consists in evaluating the energy distribution in the data looks through their GIP values. A possible choice sets κ_0 as the index in the sorted $\boldsymbol{\rho}^{(d)}$ such that the first κ_0 GIP values correspond to a preassigned percentage, say ξ , of the whole energy contained in $\boldsymbol{\rho}^{(d)}$.

C. Barycenter-Based Covariance Estimates

This section is devoted to the description of the geometric barycenters for covariance estimate that arise from the distances defined in the space of positive definite matrices [13]. More precisely, the geometric barycenters are derived from a set of basic covariance matrix estimates in turn computed from the available data looks. In this respect, denoting by \mathbf{S}_k , $k = 1, \dots, K$, the basic covariance matrix estimates, the corresponding geometric barycenter is

$$\widehat{\mathbf{M}}_d = \arg \min_{\mathbf{M}} \frac{1}{K} \sum_{k=1}^K d^2(\mathbf{S}_k, \mathbf{M}) \quad (2)$$

where $d(\cdot, \cdot) : \mathbf{A} > \mathbf{0}, \mathbf{B} > \mathbf{0} \rightarrow [0, +\infty)$ is a specific distance defined in the space of positive definite matrices.

The basic covariance estimates \mathbf{S}_k , $k = 1, \dots, K$, are directly derived from the available data looks \mathbf{r}_k as in [13]. Precisely, the basic matrix estimate \mathbf{S}_k is found as that matrix which minimizes the Frobenius norm from the rank-one covariance $\mathbf{r}_k \mathbf{r}_k^\dagger$ with the constraint $\mathbf{S}_k \geq \sigma_0^2 \mathbf{I}$ [18] (where σ_0^2 is the thermal noise power level) as the optimal solution to the following optimization problem:

$$\mathcal{P} \begin{cases} \min & \|\mathbf{r}_k \mathbf{r}_k^\dagger - \mathbf{S}_k\|^2 \\ \text{s.t.} & \mathbf{S}_k \geq \sigma_0^2 \mathbf{I}. \end{cases} \quad (3)$$

Problem \mathcal{P} admits a closed-form solution (whose proof is provided in [13]), i.e.,

$$\mathbf{S}_k = \mathbf{U}_k \mathbf{\Lambda}_k \mathbf{U}_k^\dagger \quad (4)$$

with

$$\mathbf{\Lambda}_k = \mathbf{diag}([\max(\sigma_0^2, \|\mathbf{r}_k\|^2), \sigma_0^2, \dots, \sigma_0^2]) \quad (5)$$

and \mathbf{U}_k the unitary matrix of the eigenvectors of $\mathbf{r}_k \mathbf{r}_k^\dagger$ with the first eigenvector corresponding to the eigenvalue $\|\mathbf{r}_k\|^2$.

As proved in [13], from the set of basic covariance estimates, viz., $\mathbf{S}_k \in \mathbb{C}^{N \times N}$, $k = 1, \dots, K$, the solution to the optimization problem in (2) can be uniquely found, once the specific distance has been defined. Therefore, particularizing (2) for some distances [13], [19], it is possible to derive in closed form the corresponding geometric barycenter. Specifically, let \mathbf{A} and \mathbf{B} be two positive definite Hermitian matrices, we have

- 1) Log-Euclidean distance,

$$d_L(\mathbf{A}, \mathbf{B}) = \sqrt{\text{tr}\{(\log \mathbf{A} - \log \mathbf{B})(\log \mathbf{A} - \log \mathbf{B})^\dagger\}}$$

and the corresponding log-Euclidean estimator is

$$\widehat{\mathbf{M}}_L = \exp\left\{\frac{1}{K} \sum_{i=1}^K \log \mathbf{S}_i\right\}. \quad (6)$$

- 2) Power-Euclidean distance

$$d_A(\mathbf{A}, \mathbf{B}) = \sqrt{\text{tr}\{(\mathbf{A}^\alpha - \mathbf{B}^\alpha)(\mathbf{A}^\alpha - \mathbf{B}^\alpha)^\dagger\}}$$

and the corresponding power-Euclidean estimator is

$$\widehat{\mathbf{M}}_A = \left(\frac{1}{K} \sum_{i=1}^K \mathbf{S}_i^\alpha\right)^{1/\alpha}. \quad (7)$$

The coefficient α usually lies in the set $[1/2, 1]$, and it is obvious that for $\alpha = 1$, the power-Euclidean becomes the Euclidean estimator, whereas for $\alpha = 1/2$ it takes the name of root-Euclidean estimator.

- 3) Cholesky distance

$$d_C(\mathbf{A}, \mathbf{B}) = \sqrt{\text{tr}\{[\mathbf{L}(\mathbf{A}) - \mathbf{L}(\mathbf{B})][\mathbf{L}(\mathbf{A}) - \mathbf{L}(\mathbf{B})]^\dagger\}}$$

and the corresponding Cholesky estimator is

$$\widehat{\mathbf{M}}_C = \widehat{\mathbf{\Delta}}_C \widehat{\mathbf{\Delta}}_C^\dagger \quad \text{where} \quad \widehat{\mathbf{\Delta}}_C = \frac{1}{K} \sum_{i=1}^K \mathbf{L}(\mathbf{S}_i). \quad (8)$$

Finally, the noise power level involved in (3) is recovered exploiting the cross-polarized channels \mathbf{I}_{HV} and \mathbf{I}_{VH} . As a matter of fact, they show some mismatches between each other due to noise variations if reciprocity is assumed valid [20], [21]. Hence, the thermal noise power level can be evaluated as follows:

$$\hat{\sigma}_0^2 = \frac{1}{ML} \sum_{l=1}^L \sum_{m=1}^M |\mathbf{I}_{\text{HV}}(l, m) - \mathbf{I}_{\text{VH}}(l, m)|^2. \quad (9)$$

D. Covariance Symmetry Classification

The second main step of the proposed framework is described in this section. In particular, after applying the screening procedure described in Section II-B, the full-polarimetric image is first reduced to $\bar{N} = 3$ channels fusing together \mathbf{I}_{HV} and \mathbf{I}_{VH} (substituting them by their coherent average [22]). Hence, a new filtered polarimetric data matrix $\bar{\mathbf{R}}$ of size $L \times M \times \bar{N}$ is used in place of \mathbf{R} for classifying symmetries applying the algorithm proposed in [7]. For readers' ease, in what follows, the symmetry detection algorithm of [7] is briefly described. The focus is on the classification of the special covariance/coherence structures exhibited in the presence of objects scattering with a specific symmetry [2], [6, pp. 69–72]. So, the data classification problem focuses on the exploitation of the scattering properties of the pixel under test and of its neighbors. To be precise, a dominant symmetry is associated with each pixel on the basis of the specific structure assumed by its covariance matrix. Therefore, distinguishing among four different symmetries results in the following multiple hypothesis testing problem

$$\begin{cases} H_1 : \text{no symmetry } (n = 9) \\ H_2 : \text{reflection symmetry } (n = 5) \\ H_3 : \text{rotation symmetry } (n = 3) \\ H_4 : \text{azimuth symmetry } (n = 2) \end{cases} \quad (10)$$

where in brackets the number of real scalar values describing the specific covariance has been indicated. It is worth recalling that the reflection symmetry with respect to a vertical plane can be observed over, for instance, on water surfaces in the upwind/downwind direction, plowed fields in the direction perpendicular to the row structure, on forest, snow, and so on [2]). Differently, the rotation symmetry (i.e., the covariance matrix is invariant under the rotation around an axis by any considered angle) can be experienced in the presence of dense, randomly oriented foliage. Finally, the azimuth symmetry (that is the combination of a rotation and a reflection symmetry in any plane which contains the rotation symmetry axis) can be observed in vegetated area when foliage is penetrated by the electromagnetic wave that is scattered by the horizontal branches or the vertical tree trunks [2].

Now, since (10) is a testing problem including both nested and non-nested hypotheses, the generalized maximum likelihood (GML) approach completely fails since the likelihood always assumes the highest value described by the H_1 hypothesis. This problem is overcome in [7], where a modified GML based on the MOS [10], [11], [12] is devised to deal with nested instances. This procedure consists in evaluating the decision statistic under each hypothesis, and then the order is selected as that corresponding to the minimum between the four statistics. Therefore, the decision statistics can be compactly written as follows:

$$-2 \log \left(f(\bar{\mathbf{R}} | \widehat{\mathbf{M}}^{(n)}) \right) + n \eta(n, \bar{K}) \quad (11)$$

where $f_{\bar{\mathbf{R}}}(\bar{\mathbf{R}} | \mathbf{M})$ is the complex multivariate probability density function (pdf) of the screened observable matrix $\bar{\mathbf{R}}$, with $\widehat{\mathbf{M}}^{(n)}$ the ML estimate of \mathbf{M} comprising n parameters.

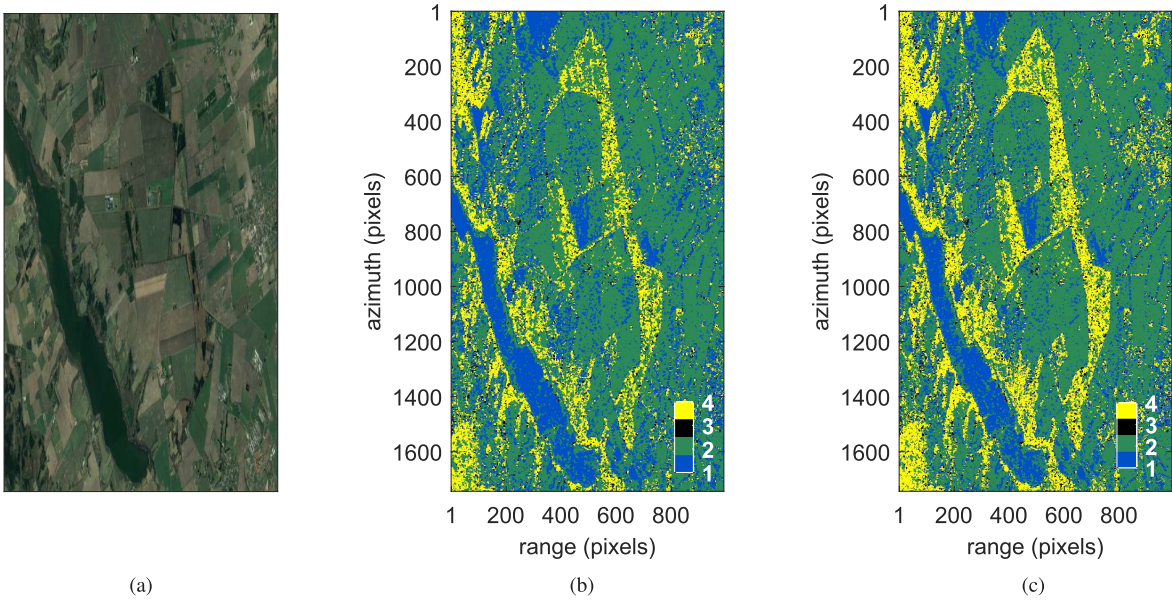


Fig. 2. Classified symmetries within the L-band EMISAR data of Foulum area with the BIC-based selectors and $K = 49$. Subplots refer to (a) optical image drawn from Google Earth©, (b) standard classifier from [7], and (c) proposed classifier with log-Euclidean barycenter.

The term $n\eta(n, \bar{K})$ is the penalty coefficient that is aimed at penalizing overfitting [11]. In this letter, the focus is on the Bayesian information criterion (BIC) setting $\eta(n, \bar{K}) = \log(\bar{K})$. However, other selection strategies can be applied as in [7].

Hence, maximizing the likelihood of $\bar{\mathbf{R}}$ under each hypothesis and substituting their respective expressions in (11), it gives rise to the following decision statistics (the interested readers can refer to [7] for detailed derivations):

1) H_1 :

$$2\bar{K} \log \det(\mathbf{S}) + 6\bar{K} + 6\bar{K} \log(\pi) + 9 \log(\bar{K})$$

with $\mathbf{S} = (1/\bar{K})\bar{\mathbf{R}}\bar{\mathbf{R}}^\dagger$ the sample covariance matrix obtained from the screened data $\bar{\mathbf{R}}$.

2) H_2 :

$$2\bar{K} \log \det(\bar{\mathbf{S}}_{1,1}) + 2\bar{K} \log(\bar{\mathbf{S}}_{3,3}) + 6\bar{K} + 6\bar{K} \log(\pi) + 5 \log(\bar{K})$$

$$\text{with } \bar{\mathbf{S}} = \mathbf{U}\mathbf{S}\mathbf{U}^\dagger = \begin{bmatrix} \bar{\mathbf{S}}_{1,1} & \bar{\mathbf{S}}_{1,3} \\ \bar{\mathbf{S}}_{3,1} & \bar{\mathbf{S}}_{3,3} \end{bmatrix}.$$

3) H_3 :

$$2\bar{K} \log \det\left(\frac{1}{2}(\bar{\mathbf{S}}_{2,2} + \mathbf{J}\bar{\mathbf{S}}_{2,2}\mathbf{J})\right) + 2\bar{K} \log(\bar{\mathbf{S}}_{1,1}) + 6\bar{K} + 2\bar{K} \log 2 + 6\bar{K} \log(\pi) + 3 \log(\bar{K})$$

with $\tilde{\mathbf{S}} = \mathbf{V}\mathbf{E}\mathbf{T}\mathbf{S}\mathbf{T}^\dagger\mathbf{E}\mathbf{V}^\dagger = \begin{bmatrix} \tilde{\mathbf{S}}_{1,1} & \tilde{\mathbf{S}}_{1,2} \\ \tilde{\mathbf{S}}_{2,1} & \tilde{\mathbf{S}}_{2,2} \end{bmatrix}$, and \mathbf{J} a permutation matrix of order 2.

4) H_4 :

$$2\bar{K} \log(\hat{\mathbf{S}}_{1,1}) + 4\bar{K} \log\left(\frac{\hat{\mathbf{S}}_{2,2} + \hat{\mathbf{S}}_{3,3}}{2}\right) + 6\bar{K} + 2\bar{K} \log(2) + 6\bar{K} \log(\pi) + 2 \log(\bar{K})$$

with $\hat{\mathbf{S}} = \mathbf{E}\mathbf{T}\mathbf{S}\mathbf{T}^\dagger\mathbf{E}$ and $\hat{\mathbf{S}}_{1,1}$, $\hat{\mathbf{S}}_{2,2}$, $\hat{\mathbf{S}}_{3,3}$ its diagonal entries, having defined the following transformation

matrices

$$\mathbf{U} = \begin{bmatrix} 1 & 0 & 0 \\ 0 & 0 & 1 \\ 0 & 1 & 0 \end{bmatrix}, \quad \mathbf{E} = \begin{bmatrix} 1 & 0 & 0 \\ 0 & 1/\sqrt{2} & 0 \\ 0 & 0 & 1 \end{bmatrix}$$

$$\mathbf{T} = \frac{1}{\sqrt{2}} \begin{bmatrix} 1 & 0 & 1 \\ 1 & 0 & -1 \\ 0 & \sqrt{2} & 0 \end{bmatrix}, \quad \mathbf{V} = \begin{bmatrix} 1 & 0 & 0 \\ 0 & 0 & j \\ 0 & 1 & 0 \end{bmatrix}.$$

Finally, the hypothesis corresponding to the minimum decision statistic is selected, that is,

$$\hat{h} = \arg \min_h \text{BIC}(h) \quad (12)$$

where $h = 1, \dots, 4$ is the index identifying the specific hypothesis. In other words, for each pixel under test, the selected structure is the one associated with $H = H_{\hat{h}}$.

III. TESTS ON MEASURED SAR DATA

In this section, the proposed methodology is validated on the L-band (1.25 GHz) coherent polarimetric dataset,² recorded by the fully polarimetric Danish airborne SAR system, electromagnetic institute SAR (EMISAR) on April 17, 1998. The SAR image of size 1750×1000 pixels has a spatial resolution of 2×2 m, with a ground range swath of about 12 km. It is representative of a scene of the Foulum area (DK), Denmark, and contains a mixed urban, vegetation, and water scene.

The optical image of the Foulum area, drawn from Google Earth© and compressed in one dimension to better match with the SAR image, is depicted as ground truth in Fig. 2(a). Furthermore, in Fig. 2(b), the classified symmetries are plotted using the BIC for the homogeneous case developed in [7]. Conversely, subplot (c) of the same figure reports the classified symmetries applying the proposed procedure with the

²Data can be downloaded at <https://earth.esa.int/web/polsarpro/data-sources/sample-datasets>

log-Euclidean barycenter (indicated as BIC-L). All the figures refer to a sliding window of size 7×7 (i.e., $K = 49$ looks), filtered with κ_0 selected in the adaptive fashion described in Section II-B1 setting $\xi = 20\%$.³ For each pixel of the scene, a specific color is associated with a specific detected symmetry, viz., blue for H_1 (no symmetry), green for H_2 (reflection symmetry), black for H_3 (rotation symmetry), and yellow for H_4 (azimuth symmetry). Obviously, pixels having the same reflection characteristics are classified in the same manner (i.e., with the same color).

Interestingly, the results highlight that lake water is classified as the absence of symmetry, forests and plants are classified with azimuth symmetry, crops and bare fields are classified with the reflection symmetry, while some buildings in urban areas are classified with a rotation symmetry. From a further visual inspection of the colored maps, it is evident that the proposed method gives some advantages over the standard classifier of [7]. In fact, analyzing the forest area, the number of pixels sharing the azimuth symmetry is reasonably higher than those in the standard case. In general, images classified with the proposed method show a sharper separation of different areas and a reduced number of isolated pixels differently classified with respect to their neighborhood in the homogeneous areas. It is also worth underlining that tests conducted with the other distances (viz., Euclidean, root-Euclidean, and power-Euclidean), not reported here for brevity, have shown results comparable to the BIC-L. Conversely, the Cholesky barycenter did not provide such good results.

IV. FINAL REMARKS

This letter has presented an enhanced framework for covariance symmetries classification in polarimetric SAR images. The devised method improves the performance of an earlier work based on the exploitation of the special structures assumed by the coherence matrix when the polarimetric returns of the pixels under test share specific symmetrical properties. More precisely, before the application of the MOS for symmetry classification, the procedure screens the most homogeneous data in the neighborhood of each pixel through the exploitation of the selective capabilities of the geometric barycenters. Furthermore, the proposed framework also takes advantage of the closed-form expression of the barycenters, thus keeping the overall computational complexity confined. Tests conducted on the L-band real-recorded polarimetric SAR data have shown the benefits of applying the screening procedure before covariance classification. As potential future research tracks, it would be interesting to test the algorithm on data recorded at different frequency bands.

ACKNOWLEDGMENT

The authors would like to thank ESA for providing the EMISAR sample data. They also would like to thank the

³Attention must be paid when setting the value ξ since for $\bar{K} < \bar{N}$, the sample matrix becomes ill-conditioned. Moreover, it should be at least $\bar{K} \geq 2\bar{N}$ to guarantee that the sample covariance matrix is a good estimate for the covariance matrix [23]. Therefore, the choice of ξ should also depend on the considered SAR data (e.g., resolution, frequency, and expected amount of non-homogeneous pixels).

Associated Editor and the Reviewers for the interesting comments and useful suggestions that have helped us to improve this letter.

REFERENCES

- [1] J. J. van Zyl, "Unsupervised classification of scattering behavior using radar polarimetry data," *IEEE Trans. Geosci. Remote Sens.*, vol. 27, no. 1, pp. 36–45, Jan. 1989.
- [2] S. V. Nghiem, S. H. Yueh, R. Kwok, and F. K. Li, "Symmetry properties in polarimetric remote sensing," *Radio Sci.*, vol. 27, no. 5, pp. 693–711, Sep./Oct. 1992.
- [3] S. R. Cloude and E. Pottier, "A review of target decomposition theorems in radar polarimetry," *IEEE Trans. Geosci. Remote Sens.*, vol. 34, no. 2, pp. 498–518, Mar. 1996.
- [4] J.-S. Lee, M. R. Grunes, T. L. Ainsworth, L.-J. Du, D. L. Schuler, and S. R. Cloude, "Unsupervised classification using polarimetric decomposition and the complex Wishart classifier," *IEEE Trans. Geosci. Remote Sens.*, vol. 37, no. 5, pp. 2249–2258, Sep. 1999.
- [5] L. Ferro-Famil and E. Pottier, "Dual frequency polarimetric SAR data classification and analysis," *Prog. Electromagn. Res.*, vol. 24, pp. 251–276, 2001.
- [6] J. S. Lee and E. Pottier, *Polarimetric Radar Imaging: From Basics to Applications*. Boca Raton, FL, USA: CRC Press, 2009.
- [7] L. Pallotta, C. Clemente, A. De Maio, and J. J. Soraghan, "Detecting covariance symmetries in polarimetric SAR images," *IEEE Trans. Geosci. Remote Sens.*, vol. 55, no. 1, pp. 80–95, Jan. 2017.
- [8] L. Pallotta, A. De Maio, and D. Orlando, "A robust framework for covariance classification in heterogeneous polarimetric SAR images and its application to L-band data," *IEEE Trans. Geosci. Remote Sens.*, vol. 57, no. 1, pp. 104–119, Jan. 2019.
- [9] T. Eltoft and A. P. Doulgeris, "Model-based polarimetric decomposition with higher order statistics," *IEEE Geosci. Remote Sens. Lett.*, vol. 16, no. 6, pp. 992–996, Jun. 2019.
- [10] Y. Selén, "Model selection," Ph.D. dissertation, Dept. Elect. Eng., Uppsala Univ., Uppsala, Sweden, Oct. 2004.
- [11] P. Stoica and Y. Selén, "Model-order selection: A review of information criterion rules," *IEEE Signal Process. Mag.*, vol. 21, no. 4, pp. 36–47, Jul. 2004.
- [12] P. Stoica, Y. Selén, and J. Li, "On information criteria and the generalized likelihood ratio test of model order selection," *IEEE Signal Process. Lett.*, vol. 11, no. 10, pp. 794–797, Oct. 2004.
- [13] A. Aubry, A. De Maio, L. Pallotta, and A. Farina, "Covariance matrix estimation via geometric barycenters and its application to radar training data selection," *IET Radar, Sonar Navigat.*, vol. 7, no. 6, pp. 600–614, Jul. 2013.
- [14] R. A. Horn and C. R. Johnson, *Matrix Analysis*. Cambridge, U.K.: Cambridge Univ. Press, 2012.
- [15] P. Chen, W. L. Melvin, and M. C. Wicks, "Screening among multivariate normal data," *J. Multivariate Anal.*, vol. 69, no. 1, pp. 10–29, 1999.
- [16] W. L. Melvin and M. C. Wicks, "Improving practical space-time adaptive radar," in *Proc. IEEE Nat. Radar Conf.*, May 1997, pp. 48–53.
- [17] E. Conte, A. De Maio, A. Farina, and G. Foglia, "Design and analysis of a knowledge-aided radar detector for Doppler processing," *IEEE Trans. Aerosp. Electron. Syst.*, vol. 42, no. 3, pp. 1058–1079, Jul. 2006.
- [18] A. Aubry, A. De Maio, and V. Carotenuto, "Optimality claims for the FML covariance estimator with respect to two matrix norms," *IEEE Trans. Aerosp. Electron. Syst.*, vol. 49, no. 3, pp. 2055–2057, Jul. 2013.
- [19] I. L. Dryden, A. Koloydenko, and D. Zhou, "Non-Euclidean statistics for covariance matrices, with applications to diffusion tensor imaging," *Ann. Appl. Statist.*, vol. 3, no. 3, pp. 1102–1123, 2009.
- [20] A. Aubry, V. Carotenuto, A. De Maio, and L. Pallotta, "Assessing reciprocity in polarimetric SAR data," *IEEE Geosci. Remote Sens. Lett.*, vol. 17, no. 1, pp. 87–91, Jan. 2020.
- [21] L. Pallotta, "Reciprocity evaluation in heterogeneous polarimetric SAR images," *IEEE Geosci. Remote Sens. Lett.*, vol. 19, pp. 1–5, 2022.
- [22] ESA. (2019). *PolSARPro (The Polarimetric SAR Data Processing and Educational Tool)*. [Online]. Available: <https://earth.esa.int/web/polsarpro/>
- [23] I. S. Reed, J. D. Mallett, and L. E. Brennan, "Rapid convergence rate in adaptive arrays," *IEEE Trans. Aerosp. Electron. Syst.*, vol. AES-10, no. 6, pp. 853–863, Nov. 1974.